Full length article

Fracture behavior and deformation mechanisms in nanolaminated crystalline/amorphous micro-cantilevers

Y.Q. Wang [a, b], R. Fritz [a], D. Kiener [a, *], J.Y. Zhang [b], G. Liu [b, **], O. Kolednik [c], R. Pippan [c], J. Sun [b, ***]

[a] Department of Materials Science, Chair of Materials Physics, Montanuniversität Leoben, Austria
[b] State Key Laboratory for Mechanical Behavior of Materials, Xi'an Jiaotong University, Xi'an, PR China
[c] Erich-Schmid-Institute of Materials Science, Austrian Academy of Sciences, Leoben, Austria

ARTICLE INFO

ABSTRACT

In order to quantify the fracture toughness and reveal the failure mechanism of crystalline/amorphous nanolaminates (C/ANLs), *in-situ* micro-cantilever bending tests were performed on Ag/Cu–Zr and Mo/Cu–Zr C/ANLs in a scanning electron microscope over a wide range of cantilever widths from several microns to the submicron scale. The results demonstrate that the fracture behavior was strongly influenced by sample size and constituent phases, respectively. The Ag/Cu–Zr micro-cantilevers failed in a ductile manner, with fracture toughnesses higher than the Mo/Cu–Zr samples that exhibited brittle failure. Both materials also displayed different cantilever width-dependences of fracture toughness. The Ag/Cu–Zr beams showed a fracture toughness that increases with the cantilever width, mainly due to a size-dependent constraining effect on the deformation of the crystalline phase. For the Mo/Cu–Zr beams, the fracture toughness decreased gradually to a low plateau as the cantilever width exceeded ~1500 nm, which can be rationalized by a transition in stress condition. The underlying fracture mechanism of the Ag/Cu–Zr micro-cantilevers was identified as the interconnection of microcracks initiated in the amorphous Cu–Zr layers, compared to a catastrophically penetrating crack propagation in the Mo/Cu–Zr samples. The discrepancy in size-dependent fracture behavior between the two material systems is discussed in terms of plastic energy dissipation of ductile phases, crack tip blunting, crack bridging and the effect of strain gradient in the plastic zone on crack propagation.

© 2019 Acta Materialia Inc. Published by Elsevier Ltd. All rights reserved.

1. Introduction

Strength and fracture toughness are two important mechanical parameters of structural materials owning to their crucial influence on the damage and failure in service of engineering components. However, the basic conflict between them is a long-existing issue, i.e., increasing the strength of metallic materials concomitantly gives rise to a deterioration of the fracture toughness, i.e. the materials become more sensitive to defects [1–5]. In general, the maximum strength and final fracture of a material are determined by its resistance against the nucleation and propagation of cracks.

The damage tolerance, i.e., the capability to sustain defects without fatal damage, is characterized by the fracture toughness and describes under which loading conditions cracks can propagate. Therefore, a fundamental understanding of the fracture toughness is extremely crucial for engineering applications of high strength materials.

Size effects on mechanical strength due to dimensional reduction have been an active topic of research in various fields, for example for refined microstructures or in thin-film materials, and some classical models/mechanisms have been proposed, for example the well-known Hall-Petch strengthening model [6,7] or the confined layer slip mechanism [8,9]. However, it remains quite challenging to measure the fracture toughness because of the small dimensions and brittleness of the thin films [10]. Especially, no standard test requirements have been developed for thin films. For instance, testing techniques such as micro-/nanoindentation [11–14], pillar indentation splitting [15–17] and indentation

scratch testing [18,19] are commonly employed to evaluate the fracture toughness of thin films on rigid substrates. However, the stress state caused in the materials during indentation based testing is complex, rendering the determination of a fracture toughness is rather difficult. In addition, the measured result actually reflects the fracture behavior of a particular film-substrate system rather than the fracture toughness of the designated thin film itself. To alleviate this substrate constraint, methods such as micro-tensile fracture [20] and micro-cantilever bending [21—23], both based on the focused ion beam (FIB) fabrication technique, are widely utilized to evaluate the actual fracture behavior of free standing thin films, since the sample geometry and loading mode can be controlled, thereby avoiding the aforementioned problems.

Meanwhile, size effects on the fracture toughness of metallic materials at small scales are attracting increasing attention [11,22,24—28]. Kang et al. [25] investigated the effect of thickness on the fracture behavior of double-edge cracked Cu foils by using tensile tests, manifesting that the fracture toughness went through a maximum with increasing thickness from 0.02 to 1.0 mm. Correspondingly, the failure mode changed from a more brittle to a rather ductile mechanism, since the shear fracture controlled by inner micro-defect transferred to a slip plasticity dominated by stress tri-axiality and void growth. Lu et al. [28] also disclosed a similar specimen thickness effect on the fracture behavior in electrodeposited columnar-grained Cu with oriented nanotwins. At smaller sample thicknesses, plane stress condition prevailed ahead of the crack, while the crack tip was mainly under plane strain condition once the thickness exceeded a critical value where the fracture toughness reached a maximum. This transition of stress conditions was attributed to the interactions between dislocations and grain/twin boundaries. Generally, the crack is strongly constrained in plane strain condition due to a small plastic zone size around the tip, leading to brittle fracture behavior and a lower, size-independent fracture toughness in sufficiently thick samples. With reducing the sample dimensions, plane stress becomes more and more dominant in thin samples, accompanied by ductile fracture owing to the large plastic zone and increasingly higher, size-dependent fracture toughness values.

Recent investigations on the fracture toughness of thin films mainly focused on hard and brittle ceramic coatings, such as oxide, nitride and oxynitride thin films [21,22,29,30], which usually exhibit brittle fracture and inferior fracture toughness. Thus, enhancing the toughness of brittle thin films and revealing the toughening mechanisms is becoming more significant for promoting the mechanical performance. One promising method is to engineer ductile metals in combination with hard coatings into multilayered composites. Besides adding a ductile phase, this also introduces large amounts of interfaces that can serve to impede crack propagation, e.g. crystalline/crystalline nanolaminates (C/CNLs) [31—35] or crystalline/amorphous nanolaminates (C/ANLs) [36—40]. Although extensive efforts have been devoted to explore the mechanical reinforcing and toughening performance by designing multilayered composites, only few experimental studies reported the deformation and failure of nanolaminated thin films, mostly due to challenges arising in micromechanical testing necessitated by the restrictions in sample dimension [22,41]. For example, Manoharan et al. [41] measured the fracture toughness of 300 nm thick Ti/TiN multilayers by using an *in-situ* bending test, and observed stable crack growth with micro-cracking and branching events preceding final fracture. Specifically, the interface category, the sample size and the mutual constraint between constituent nanolayers can have significant influence on the fracture toughness and deformation behavior in metallic nanolaminates. Therefore, detailed analytical and mechanical understanding of deformation mechanisms related to fracture in small-scale nanolaminates is important for successful design of nanocomposite materials with desirable combinations of high strength and toughness.

The purpose of this work is to study the size- and constituent-dependent fracture toughness of two kinds of C/ANLs, i.e., Ag/Cu—Zr and Mo/Cu—Zr with identical constituent layer thickness of ~50 nm, by means of notched micro-cantilevers. The influence of the micro-cantilever size, ranging from several micrometers down to the submicron scale, and the constraining effect from the adjacent constituent layers are systematically investigated. The samples are fabricated by FIB and subsequently tested using an *in-situ* microindenter mounted in a scanning electronic microscope (SEM). This allows for a distinct visualization of the crack propagation process that is beneficial to the analysis of crack resistance behavior and the determination of fracture toughness quantities. Through dissecting the experimental results, we attempt to clarify the fracture behavior and the toughening mechanism in terms of the interaction between microcrack and constituent layers in the C/ANLs, offering guidance for an improved structural design of nanolayered composites.

2. Experimental procedure

2.1. Materials preparation and characterization

Crystalline/amorphous Ag/Cu—Zr and Mo/Cu—Zr nanolaminates with equal thickness of ~50 nm for the crystalline and amorphous layers were deposited on acetone-cleaned (100) silicon substrates by using magnetron sputtering at room temperature. Pure Cu (99.995%) and Zr (99.99%) targets (direct current sputtering) were used to prepare the amorphous Cu—Zr nanolayers, and pure Ag (99.99%) and Mo (99.95%) targets (radio frequency sputtering) for the crystalline Ag and Mo nanolayers, respectively. The composition of the amorphous Cu—Zr nanolayers is $Cu_{75}Zr_{25}$, and the total thickness of the two nanolaminates is ~2 μm. Before the deposition process, the chamber was evacuated to a base pressure of $<3.0 \times 10^{-7}$ Torr, and 7.5×10^{-3} Torr of Ar was maintained. In all cases, the amorphous layer was firstly deposited on the substrate, and the cap layer was constantly a crystalline metal. The microstructure and elemental composition of the as-deposited C/ANLs are confirmed by transmission electron microscopy (TEM) conducted on a JEOL JEM-2100F microscope.

2.2. Fabrication of the nanolaminated micro-cantilevers

To evaluate the fracture toughness of the two kinds of C/ANLs on a small scale, micro-cantilevers with pre-notches were prepared by two steps. First, the samples to be studied were extracted from a region in the middle of the Si substrates to avoid any influence from inhomogeneous film deposition near the wafer edge. Then, a narrow freestanding fillet on the sample is prepared using broad beam ion milling [42]. The experimental procedure in detail can be found in Ref. [43]. The second step concerns the final shaping of the cantilevers by utilizing FIB milling performed in a LEO 1540XB workstation (Zeiss, Oberkochen, Germany). All the rectangular cantilevers in both of the C/ANLs were machined with dimension of L ~15 μm in length, W ~4 μm in height. This is twice the multilayer thickness to enable a tensile stress state of the nanolaminates. The dimension of L generally does not impact the measured fracture toughness unless the stress gradient in front of the crack is changed notably [44] by changing L by significant amounts, while the influence of W would be very limited within the margin of error (less than 6.0% in this work). This is commonly accounted for by the geometry factor $f(a/W)$, see below. Various cantilever widths of B ~0.5—3.5 μm were realized to study the thickness dependences.

Representative as-fabricated microcantilevers of Ag/Cu−Zr and Mo/Cu−Zr and the related geometrical dimensions are displayed in Fig. 1. Subsequently, the front, back and bottom of the specimens were milled from the top and the side, respectively. Naturally, one end of the cantilever was fixed in the bulk material, while the other was free for later loading with a nanoindenter. Coarse milling currents of 2 nA−500 pA were used to fabricate the rough shape, followed by the final polishing of the cantilevers to the required dimensions with lower ion currents from 200 pA to 50 pA to minimize the damage caused by Ga$^+$ implantation [45]. Prior to the final polishing, the wedge-shaped notches were introduced at about 2 μm distance from the support to avoid undesired plastic deformation of the base. All notches were fabricated using the line-milling mode with a low ion current of 10 pA, with the ion beam direction parallel to the loading direction, allowing a defined and reproducible notch depth of a ~450 nm. The characteristic dimensions of the testing samples including typical experimental variation were measured from SEM images and are outlined in Table 1.

2.3. Bending testing of the nanolaminated micro-cantilevers

All the cantilever bending tests were performed *in situ* inside a LEO 982 scanning electronic microscope (SEM, Zeiss, Oberkochen, Germany) using an UNAT-SEM Indenter (Zwick GmbH & Co. KG, Ulm, Germany) equipped with a diamond wedge tip (Synton MDP, Nidau, Switzerland). The fracture experiments were performed in displacement controlled mode with a constant loading and unloading rate of 15 nm s^{-1} for all cantilevers. During each *in situ* experiment, the applied displacement and corresponding force were recorded with a correlated video in terms of SEM image sequences at the same time.

In order to evaluate the conditional fracture toughness K_Q of the micro-cantilevers, the maximum force F_{max} was measured from the load-displacement curve. The stress intensity factor K of the cantilever specimens used for the evaluation of the fracture toughness parallel to the bending direction can be calculated following linear elastic fracture mechanics [46]:

$$K = \frac{FL}{BW^{3/2}} f\left(\frac{a}{W}\right) \tag{1}$$

where F is the load applied by the indenter, and the function $f(a/W)$ is the geometry factor that can be written as:

$$f\left(\frac{a}{W}\right) = 1.46 + 24.36\left(\frac{a}{W}\right) - 47.21\left(\frac{a}{W}\right)^2 + 75.18\left(\frac{a}{W}\right)^3 \tag{2}$$

as derived from two-dimensional Abaqus finite element simulations [29]. From the test record, the maximum force F_{max} was taken to determine the fracture toughness K_Q.

3. Results

3.1. Morphology and microstructure of the nanolaminated cantilevers

Representative SEM images of as-fabricated rectangular Ag/Cu−Zr with $B = 2.14$ μm and Mo/Cu−Zr with $B = 2.15$ μm microcantilevers with pre-notches are shown in Fig. 1. Local magnified notch regions from the side view inserted in Fig. 1(a) and (b) manifest the clear wedge-shaped notch geometry and the nano-layered modulation structure. The top and side view of the cantilevers shown in Fig. 1(c) and (d) demonstrate that the FIB-fabricated notches are perpendicular to the profile, avoiding the effect of notch inclination. Besides, we can clearly distinguish the interface between C/ANLs and Si substrate, which is almost located at the neutral plane to guarantee the tensile stress state of C/ANLs during bending.

Typical microstructures of as-deposited Ag/Cu−Zr and Mo/Cu−Zr C/ANLs examined *via* high resolution TEM (HRTEM) are
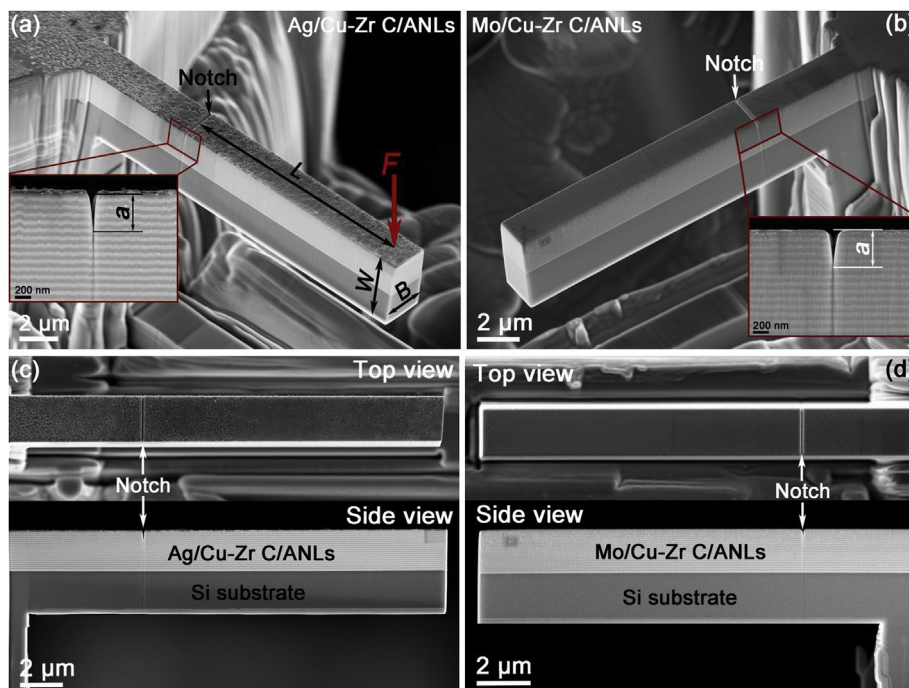

Fig. 1. Representative inclined SEM images of the micro-cantilevers in (a) Ag/Cu−Zr with $B = 2.14$ μm and (b) Mo/Cu−Zr C/ANLs with $B = 2.15$ μm, respectively. Inserts are detailed pre-cracks in a side view. (c−d) Top view and side view of the notched micro-cantilevers in the Ag/Cu−Zr and Mo/Cu−Zr C/ANLs.

Table 1
Specimen dimensions shown in Fig. 1, measured maximum force and deflection from the load-displacement curves, calculated fracture toughness and plastic zone size of crack tip.

Materials	B (μm)	L (μm)	W (μm)	A (nm)	F_{max} (μN)	U (μm)	K_Q (MPa·m$^{1/2}$)	$K_{Q, CTOD}$ (MPa·m$^{1/2}$)	R_p (nm)
Ag/Cu−Zr	0.50	15.58	3.52	450	88	1.50	1.64 ± 0.12	1.69 ± 0.04	268 ± 43
	0.99	14.03	3.73	450	255	1.43	1.93 ± 0.06		369 ± 30
	1.43	11.86	3.93	460	525	1.53	2.14 ± 0.04	2.17 ± 0.05	453 ± 30
	2.05	15.15	4.07	530	650	1.78	2.34 ± 0.04		543 ± 34
	2.14	14.01	3.88	500	700	1.87	2.38 ± 0.04	2.39 ± 0.07	564 ± 35
	3.03	15.72	4.10	530	980	1.67	2.43 ± 0.03		584 ± 34
Mo/Cu−Zr	0.65	12.69	3.93	430	160	0.45	1.47 ± 0.07	−	38 ± 4.2
	0.98	15.61	4.42	430	220	0.59	1.30 ± 0.04	−	30 ± 2.7
	1.67	14.32	3.69	420	225	0.58	1.02 ± 0.03	−	18 ± 1.5
	2.15	13.59	3.91	410	335	0.55	0.98 ± 0.02	−	17 ± 1.3
	2.70	15.85	4.05	420	340	0.57	0.87 ± 0.02	−	13 ± 1.0
	3.59	16.10	4.25	410	540	0.78	0.95 ± 0.01	−	16 ± 1.1
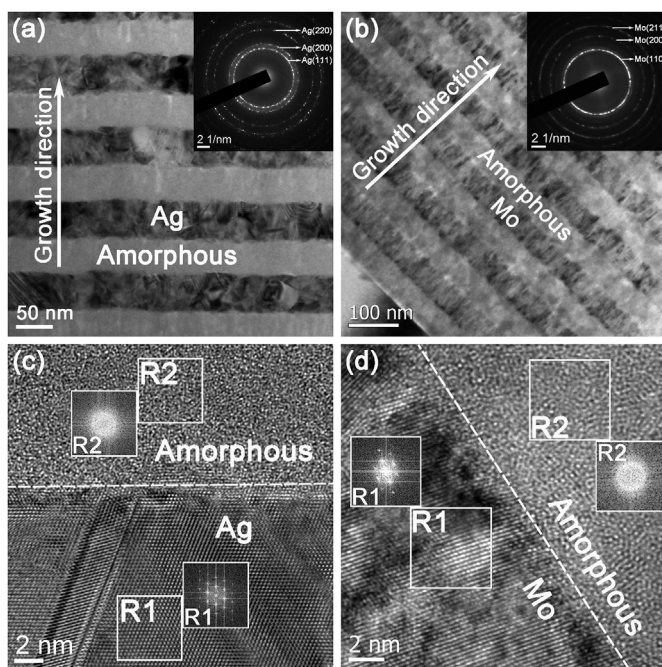
Fig. 2. (a−b) Typical cross-sectional TEM microstructures of as-deposited Ag/Cu−Zr and Mo/Cu−Zr C/ANLs with the corresponding selected area diffraction patterns (SADPs) inserted. (c−d) Localized high resolution TEM images at crystalline/amorphous interfaces and fast Fourier Transforms (FFTs) from constituent layers indicating the crystalline and amorphous structure, respectively.

presented in Fig. 2. The modulated layered structure with distinct crystalline/amorphous interfaces (CAIs) between crystalline metal and fully amorphous Cu−Zr layers is evident in the as-deposited C/ANLs, as displayed in Fig. 2(a−b). In addition, the Ag layers show clear columnar grains with an average grain size comparable to the layer thickness, while the Mo layers display undistinguished fine-columnar nanograins. The corresponding selected area diffraction patterns (SADPs) in the inset of Fig. 2(a−b) definitely demonstrate polycrystalline diffraction spots corresponding to Ag (111), Ag (200), Ag (220) and Mo (110), Mo (200), Mo (211), respectively. Also the diffuse amorphous ring arising from the Cu−Zr nanolayers are evident. Fig. 2(c−d) show the localized regions of distinct crystalline/amorphous interfaces and the fast Fourier transform (FFT) analyses in each constituent layer, indicating the ordered crystalline structure in Ag and Mo layers and the disordered amorphous structure in Cu−Zr layers.

### 3.2. Crack propagation within the nanolaminated cantilevers

Different crystalline constituent layers (i.e., Ag and Mo) incorporated between the amorphous Cu−Zr layers can exhibit different effects on the microcrack nucleation and propagation. Fig. 3(a) and (b) illustrate the respective microcrack propagation process of a Ag/Cu−Zr cantilever with $B = 1.43$ μm and a Mo/Cu−Zr cantilever with $B = 0.98$ μm, *in situ* monitored during a bending test. With the electron beam continuously scanning the sample side throughout the test, the entire fracture process was recorded, and several snapshots from the movies are shown in Fig. 3(a) and (b).

For the Ag/Cu−Zr micro-cantilever (Fig. 3(a)), with increasing deflection the crack started to initiate at the tip of the pre-notch and propagated along the notch direction, but was blocked by the ductile Ag layer. Immediately following, distinct and gradual necking occurred in the Ag layer (indicated by the blue arrow), accompanied by brittle fracture of the adjacent Cu−Zr amorphous layer (shown by the yellow arrow). Then, the crack tip was again blunted within the subjacent Ag layer, yet the first necked Ag layer still did not completely fracture due to good plastic deformability. With further bending deflection, more Cu−Zr layers failed, while the adjacent Ag layers still kept connection, forming a chain-type crack propagation. Finally, once the growing stress intensity ahead of the crack tip could not be balanced by the ductile Ag layer upon progressively applied stress, the entire Ag/Cu−Zr micro-cantilever fractured through the crack bridges and remaining material.

For the Mo/Cu−Zr micro-cantilever (Fig. 3(b)), it is challenging to distinctly observe the nucleation and propagation of a micocrack due to the rapid speed of crack expansion. From the snapshots, we can just note a slight opening of the pre-notch before fracture. Once the crack initiation occurred, it quickly penetrated throughout the whole micro-cantilever, resulting in catastrophic fracture. Generally, the final fracture surface appears overall rather straight, as expected for brittle fracture behavior. Nonetheless, the *in situ* images document that there is local crack deflection and bridging during the propagation, contributing to the toughening of the materials.

3.3. Mechanical response of the nanolaminated cantilevers

Fig. 4(a) and (b) show the load-deflection curves of the micro-cantilevers in Ag/Cu−Zr and Mo/Cu−Zr C/ANLs, respectively. Both kinds of C/ANL micro-cantilevers exhibit similar mechanical response, i.e., the slope of the loading curves increases with raising the sample size. Here, it should be pointed out that the fluctuation
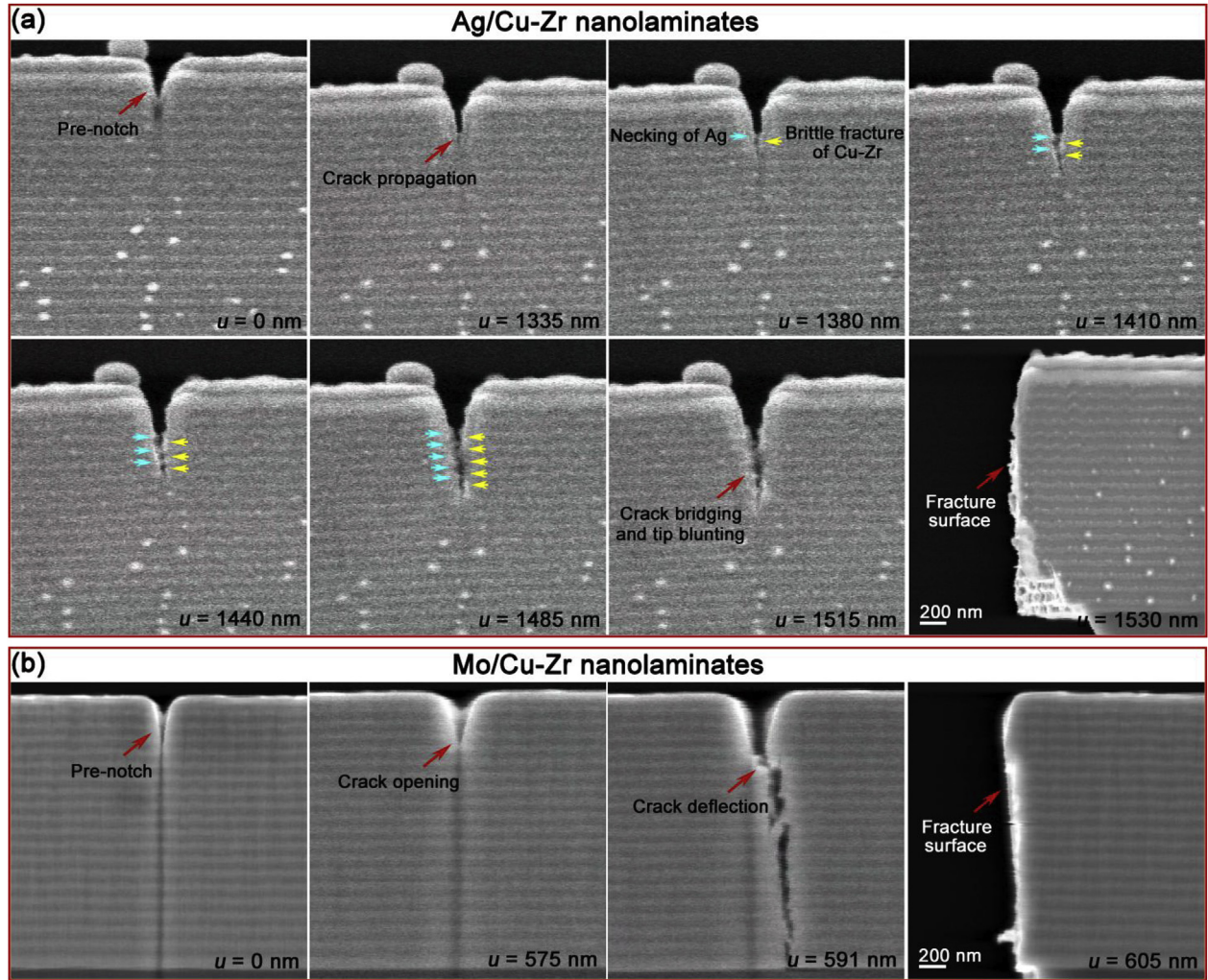
Fig. 3. Fracture behavior and corresponding microcrack evolution of the C/ANLs micro-cantilevers with deflection u. Still frames extracted from the recorded movies in (a) Ag/Cu–Zr with $B = 1.43$ μm and (b) Mo/Cu–Zr C/ANLs with $B = 0.98$ μm. The blue arrows indicate necking of Ag layers and yellow arrows brittle fracture of Cu–Zr layers. Obviously, ductile fracture occurred in the Ag/Cu–Zr sample because the crack that nucleated in Cu–Zr layers was bridged in the remaining material, while brittle fracture occurred in the Mo/Cu–Zr with rapid propagation of the crack. (For interpretation of the references to color in this figure legend, the reader is referred to the Web version of this article.)
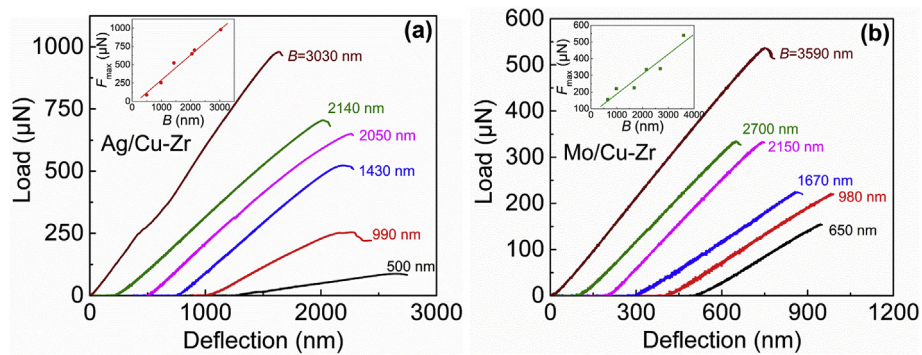
Fig. 4. Mechanical test records of load-displacement curves for the (a) Ag/Cu–Zr and (b) Mo/Cu–Zr C/ANLs with different cantilever width B. The inserts are the dependence of maximum load F_{max} on the cantilever width B. With decreasing B, the Ag/Cu–Zr micro-cantilevers show more apparent plastic deformation, while an inverse situation occurs in the Mo/Cu–Zr samples.

on the curve of Ag/Cu–Zr sample with $B = 3030$ nm was caused by an occasional minor tip sliding of the indenter during loading process, which quickly recovered to normal state before the sample fractured, thus having no effect on the calculation of fracture toughness. The inserted figures show the dependence of maximum load F_{max} on cantilever width B. As expected for a linear elastic material, F_{max} of the cantilever linearly increases with increasing B for both of the C/ANLs, and the failure loads of the soft Ag/Cu–Zr are

larger than that of the hard Mo/Cu−Zr C/ANLs for corresponding B. In addition, the cantilever in the Ag/Cu−Zr system displayed more apparent plastic deformation with decreasing the beam width B, while an opposite variation is evident in the Mo/Cu−Zr C/ANLs.

Under the assumption of linear elastic fracture behavior, using equations (1) and (2) with the measured specimen dimensions given in Table 1, the stress intensity factor K at the crack tip during bending can be estimated for different cantilever widths as shown in Fig. 5(a) and (b). Interestingly, compared with the load-deflection curves in Fig. 4, the mechanical response of K is similar to that of load for Ag/Cu−Zr cantilevers, while it exhibits a completely inverse variation in the Mo/Cu−Zr cantilevers. That is to say, with increasing B, stress intensity K gradually increases in Ag/Cu−Zr C/ANLs, whereas it decreases in Mo/Cu−Zr.

The conditional fracture toughness K_Q calculated from the maximum load F_{max} as a function of cantilever width B is presented in Fig. 6(a) for both kinds of C/ANLs cantilevers. As mentioned, the K_Q gradually increased in Ag/Cu−Zr cantilevers with increasing cantilever width B (Fig. 6(a) upper part). However, there exists an inverse K_Q variation for Mo/Cu−Zr cantilevers (Fig. 6(a) bottom part), i.e., K_Q decreased drastically as B increased to a value of ~1500 nm, above which it almost reached a low constant value. Generally, the Ag/Cu−Zr micro-cantilevers presented a higher fracture toughness K_Q than the Mo/Cu−Zr ones. This constituent- and size-dependent fracture toughness of C/ANLs may be related to the stress state ahead of the crack tip and the interaction with microstructural features, which will be addressed in the next section.

Generally, a plane stress condition fully develops if the beam width B is smaller than the plastic zone size R_P in plane strain loading. In order to analyze the resistance of crack propagation during bending, the plastic zone size ahead of crack tip in a plain strain state can be estimated according to the following equation [27,28]:

$$R_P = \frac{1}{3\pi}\left(\frac{K_Q}{\sigma_y}\right)^2 \tag{3}$$

where σ_y is the yield strength of the specimen. Here, for the Ag/Cu−Zr specimens $\sigma_{y,\ Ag/Cu−Zr} = 1.03$ GPa and for the Mo/Cu−Zr specimens $\sigma_{y,\ Mo/Cu−Zr} = 2.47$ GPa as deduced from nano-indentation [47]. Both the calculated R_p depending on cantilever width B are shown in Fig. 6(b) for presumed plane strain conditions, respectively. Obviously, the variation of calculated R_p in each kind of C/ANLs is analogous to the trend of fracture toughness K_Q. Moreover, for the Ag/Cu−Zr cantilevers, R_p is in any case larger than several layer thicknesses, thus local fluctuations in material properties between layers will be of little influence to the material behavior. Contrarily, for the Mo/Cu−Zr cantilevers the estimated plastic zone is smaller than individual layers, and material

inhomogeneity influences on fracture properties might arise [48,49].

Going beyond the simple measurement of fracture toughness via linear-elastic fracture mechanics, it is also possible to assess the fracture toughness by using elastro-plastic fracture mechanics methods such as the crack tip opening displacement (CTOD). The benefit of this is its extended validity compared to linear elastic fracture mechanics. CTOD is used on materials that can exhibit some plastic deformation before failure occurs causing the tip to stretch open. For the Mo/Cu−Zr micro-cantilevers, it is hard to observe the crack propagation due to the almost immediate cata-strophically brittle fracture, so here we just describe the crack extension behavior of Ag/Cu−Zr micro-cantilevers. The value of CTOD generally reflects the resistance of a material to the propa-gation of a crack. By measuring the CTOD and corresponding crack extension Δa of three representative samples, we obtained the relationships between CTOD and Δa and deflection u, as shown in Fig. 7(a) and (b). Obviously, CTOD notably increases with crack extension Δa and deflection u. According to the standard [50], the maximum allowed values of CTOD and crack extension Δa are (W-a)/20 and (W-a)/4, which are calculated as $CTOD_{max}$ ~ 170 nm and Δa_{max} ~ 850 nm, respectively, and indicated as red dashed lines in Fig. 7. Within these limits, we find two stages for the crack prop-agation. Following the evaluation method proposed by Wurster et al. [46] for small scale samples, linearly fitting the initial blunting and final propagation stage of each CTOD-Δa curve, the point of intersection of the two fitted lines is the conditional crack tip opening displacement $CTOD_Q$. Then, the elasto-plastic fracture toughness $K_{Q,\ CTOD}$ is estimated by Ref. [46]:

$$K_{Q,\ CTOD} = \sqrt{\sigma_y \cdot E \cdot CTOD_Q} \tag{4}$$

where σ_y and E are the yield strength and elastic modulus of Ag/Cu−Zr C/ANLs, respectively, measured to be 1.03 GPa and 95 GPa by nanoindentation [47]. With raising cantilever width B, we find increasing conditional $CTOD_Q$ values of 29 nm, 48 nm and 58 nm, respectively, relating to elasto-plastic fracture toughness values of 1.69 ± 0.04 MPa m$^{1/2}$, 2.17 ± 0.05 MPa m$^{1/2}$ and 2.39 ± 0.07 MPa m$^{1/2}$. These values are in line with the data in Fig. 6(a). In addition, careful examination from Fig. 7(b) indicates that the thicker beam indeed has a longer blunting stage before crack growth sets in, further supporting the calculated conditional $CTOD_Q$ results above. The deflection displacement u, conditional fracture toughness K_Q, $K_{Q,\ CTOD}$ and plastic zone size R_P are summarized in Table 1.

3.4. Fractography of the nanolaminated cantilevers

Fig. 8 shows the fracture morphology of a representative Ag/Cu−Zr micro-cantilever with $B = 2.14$ μm. From the side view (Fig. 8(a)), we see that the crack propagated perpendicular to the C/A interfaces along the pre-notch, with no obvious declination or zigzag. From the front view (Fig. 8(b)), four zones are presented evidently, i.e., the film surface, pre-notch, fracture surface of nanolaminates and Si substrate. Next, we will primarily analyze some details of the fracture surfaces of the nanolaminates.

Representative fracture surface morphologies of Ag/Cu−Zr with $B = 2.14$ μm and Mo/Cu−Zr with $B = 3.59$ μm micro-cantilevers are displayed in Fig. 9. At the pre-notch zone, the layered modulation structure can be distinguished clearly. After bending fracture, we can still observe the nanolayered structure at the fracture surface zone of Ag/Cu−Zr micro-cantilever, while this is absent in the Mo/Cu−Zr cantilever, compare Fig. 9(a) and (b). Fig. 9(c) and (d) provide magnified observations of the red dashed regions in Fig. 9(a) and (b). Globally, both the fracture surfaces of micro-cantilevers are flat, but
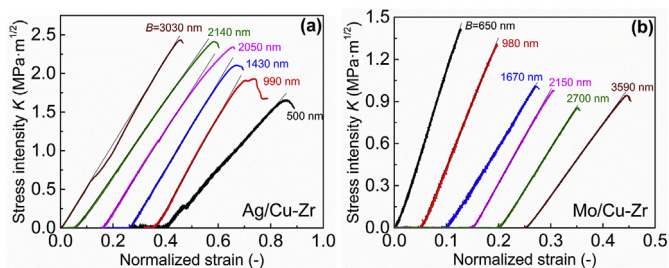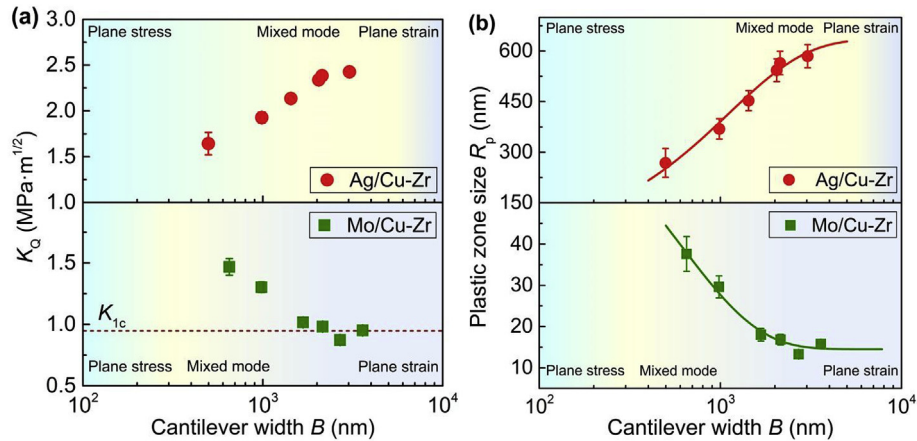

Fig. 5. Stress intensity factor K vs. deflection curves of the (a) Ag/Cu−Zr and (b) Mo/Cu−Zr C/ANLs with different cantilever width B. Interestingly, the stress intensity factor K increases with raising B in Ag/Cu−Zr, yet it decreases in Mo/Cu−Zr C/ANLs.

Fig. 6. Cantilever width B-dependent fracture toughness K_Q (a) and calculated plastic zone size of crack tip R_p (b) in Ag/Cu−Zr (upper part) and Mo/Cu−Zr (bottom part) C/ANLs. The three different stress state regions, i.e., plane stress, mixed state and plane strain, are distinguished by different colors in (a) and (b). Both kinds of C/A micro-cantilevers display completely opposite variations in K_Q and R_p with cantilever width B, respectively. (For interpretation of the references to color in this figure legend, the reader is referred to the Web version of this article.)
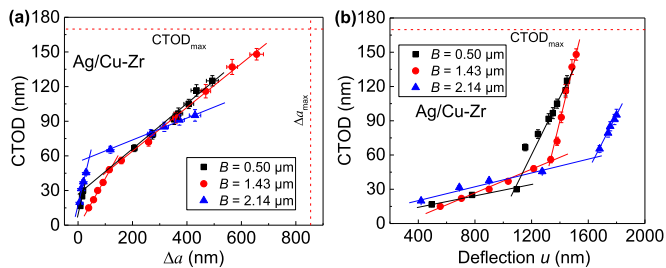
Fig. 7. CTOD as a function of (a) crack extension Δa and (b) deflection u in Ag/Cu−Zr cantilevers with $B = 0.50\,\mu m$, $1.43\,\mu m$ and $2.14\,\mu m$. Red dashed lines indicate the maximum allowances of CTOD and crack extension Δa. There are two apparent stages for the initial blunting and unstable crack propagation, respectively. The intersection point of the two fitted lines for the two stages is defined as the conditional $CTOD_Q$, which is used to estimate the elastro-plastic fracture toughness. (For interpretation of the references to color in this figure legend, the reader is referred to the Web version of this article.)
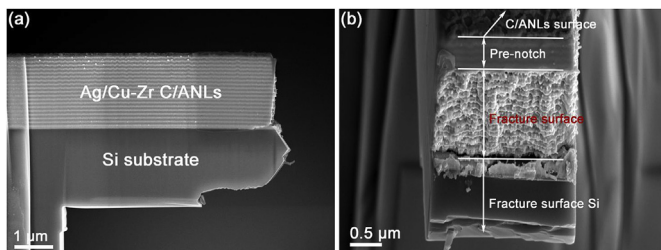
Fig. 8. Representative side view (a) and front view (b) of the Ag/Cu−Zr C/ANLs cantilever with $B = 2.14\,\mu m$ after fracture. The fracture zone of C/ANLs is clearly visible.

locally Ag/Cu−Zr shows obvious stretching, while Mo/Cu−Zr only some steps from deflection. Focusing on the Ag/Cu−Zr system, the soft Ag layers were pulled out and necking occurred, while the amorphous Cu−Zr layers exhibit a columnar fractography without visible plastic deformation features. Notably, several bright particles appeared in the amorphous Cu−Zr layers, which are likely droplets of Cu−Zr intermetallics produced during the rapid crack propagation [51]. Contrarily, for the Mo/Cu−Zr micro-cantilevers the fracture surface has no layered structure. There are, however, much more droplet particles distributed on the fracture surface, as indicated by red arrows in Fig. 9(d). Moreover, the fractograph contains

some unconspicuous columns (shown by the yellow arrows) and few fault scarps (shown by the green arrows) that indicate some crack deflection during propagation, in line with Fig. 3(b).

4. Discussion

4.1. Fracture mechanisms of the C/ANL micro-cantilevers

From the fractography of the two different C/ANL cantilevers, one can clearly observe that amorphous Cu−Zr engineered with crystalline Ag or Mo constituent layers exhibited completely different failure behavior, i.e., brittle fracture in Mo/Cu−Zr but ductile fracture in Ag/Cu−Zr micro-cantilevers. That is closely related to the plastic deformability of the constituent nanolayers [52,53].

In the Mo/Cu−Zr multilayered beams, the fracture surface exhibits a somewhat blocky surface that seems to correlate to some extent to the columnar grain boundaries in the Mo layer and the horizontal interfaces between the different layers. However, it is surprising that the layered modulation structure is barely evident on the fracture surface. In terms of the influence of the layered heterogeneous structure on Si, there will be a certain undulation in actual crack driving force between the nanolayers, being higher in Mo and lower in Cu−Zr compared to a homogeneous material. Furthermore, K_{1c} will be globally somewhat underestimated, as the modulus of the multilayers is slightly larger than that of Si, which could give rise to a certain crack tip shielding contribution [54,55]. While these influences could be treated, the minor details are not the dominant contribution to the observed changes and will therefore not be addressed in detail. Rather, we will for the sake of simplicity treat the multilayers as a homogenous medium.

Notably, the fracture toughness in this system is ~1.0 MPa m$^{1/2}$, which is nearly the Griffith toughness of Mo. Thus, we can conclude that the fracture process resembles the nearly ideal grain boundary fracture of Mo and Cu−Zr, where the Mo grain boundary structure dominates the crack path geometry, both in the Mo as well as the Cu−Zr layers, respectively. Due to the low fracture toughness values also no significant dissipation of energy is expected in the Cu−Zr layers besides the decohesion energy, which would result in a local crack resistance. Additionally, the local driving force is smaller in the Cu−Zr layers due to the shielding of the elastically stiffer and stronger Mo. As the nucleated crack rapidly traverses the brittle Mo layer and penetrates the Cu−Zr layer, the strong stress intensity of
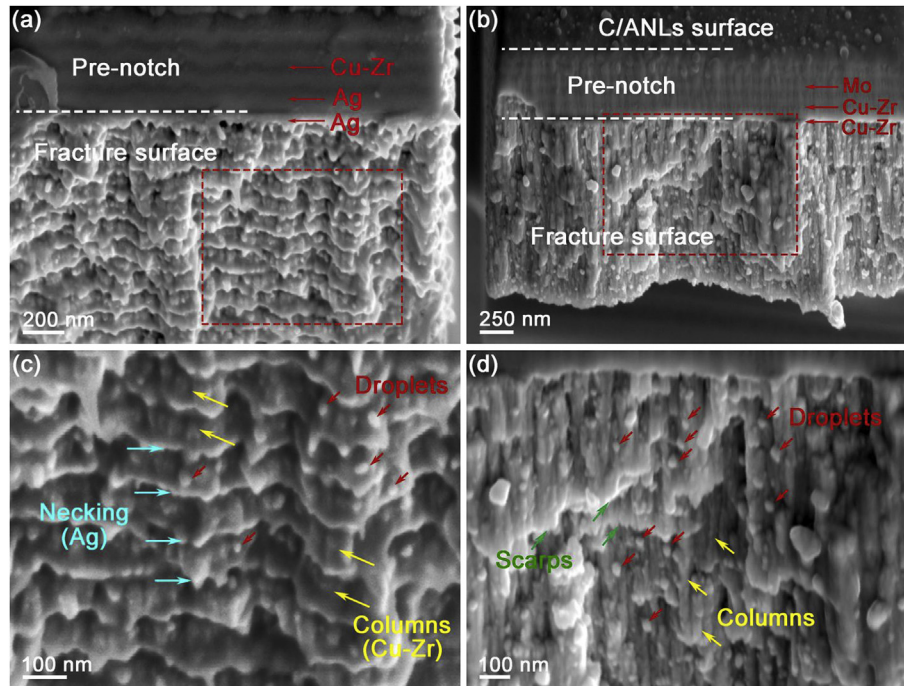
Fig. 9. Representative surface morphology of (a) Ag/Cu−Zr with $B = 2.14\,\mu m$ and (b) Mo/Cu−Zr C/ANLs with $B = 3.59\,\mu m$ after fracture. (c) and (d) are magnified images of the red dashed regions in (a) and (b). The Ag/Cu−Zr presented ductile fracture features with obvious necking in Ag layers and column-like in Cu−Zr layers, while the Mo/Cu−Zr exhibited a brittle fractograph. (For interpretation of the references to color in this figure legend, the reader is referred to the Web version of this article.)

the crack tip could induce the observed droplets on the fracture surface, which would also dissipate some energy. Hence, once a microcrack nucleates, the instantaneous catastrophic fracture occurs (see the schematic images in Fig. 10(a)). In other words, the brittle fracture of Mo/Cu−Zr micro-cantilevers is determined by the initiation of a nanoscale crack.

With regard to the Ag/Cu−Zr micro-cantilevers, nanocrystalline Ag as the soft-ductile phase dominates the plastic deformation, while amorphous Cu−Zr as the hard-brittle phase enhances the extension of microcracks. We can observe the fracture behavior

from the *in situ* SEM bending process, where the crack preferentially initiated in amorphous Cu−Zr layers and then gradually propagated to subsequent Cu−Zr layers with Ag layers bridging over the crack. That is to say, the occurrence of crack nucleation does not determine the final fracture of the samples. As shown schematically in Fig. 10(b), the Cu−Zr phase seems to exhibit a similar brittle characteristic as in the Mo/Cu−Zr case. However, the Ag layers fail by a necking process where the required energy is predominantly determined by the necking process of the 50 nm Ag layer. As expected in the case of complete necking, the critical CTOD
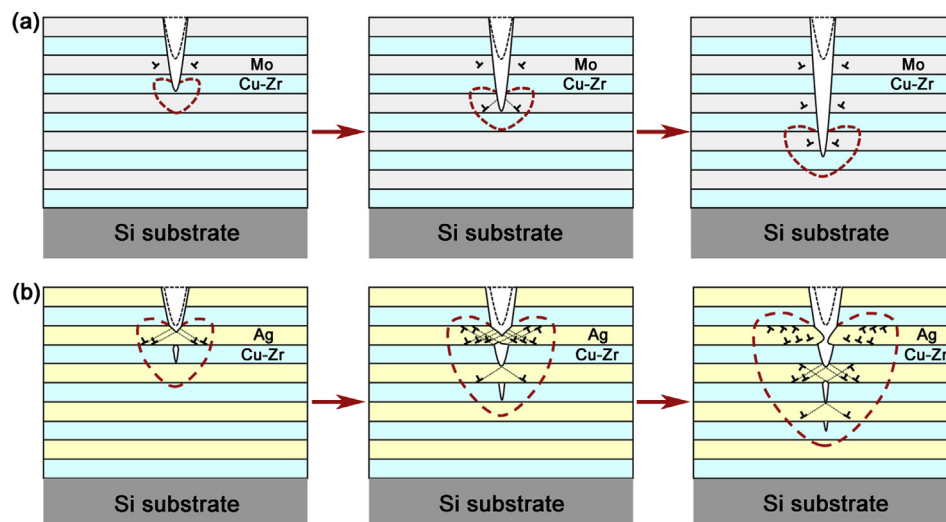
Fig. 10. Schematic images of fracture mechanism in (a) Mo/Cu−Zr and (b) Ag/Cu−Zr C/ANL micro-cantilevers, demonstrating interaction of the crack with the constituent layers and crystalline/amorphous interfaces. The profile of initial crack and the plastic zone ahead of crack tip are outlined in black and red dashed lines, respectively. With increasing deflection, crack extension in Mo/Cu−Zr is almost unobstructed with negligible plastic deformation in crystalline Mo layers, while a larger plastic zone emerges in Ag/Cu−Zr due to significant deformation of ductile Ag layers and consequent toughening via crack bridging. (For interpretation of the references to color in this figure legend, the reader is referred to the Web version of this article.)

(Fig. 7) is somewhat smaller than the thickness of the layer. Dislocations initiate at the crack tip, the crystalline/amorphous interface or a grain boundary and glide along the slip planes, thus the crack tip is shielded in the Ag nanolayer. With increasing deformation, more and more dislocations will aggregate at the crystalline/amorphous interface and the high local stresses will lead to failure of the amorphous Cu−Zr layer, causing a brittle columnar-like fractograph in the Cu−Zr layers (indicated by yellow arrows in Fig. 9(c)). However, the crack will be blunted and arrested by the soft Ag layers which still do not fracture but keep necking at this moment. Thus, the Ag layers act as bridging agent, deforming plastically and preventing catastrophic fracture of the sample. The fractural mode is accordingly not the continuous extension of a crack, but the interconnection of several microcracks initiated in the amorphous Cu−Zr layers. Therefore, the toughening mechanism can be attributed to plastic dissipation within the ductile Ag layer, crack tip blunting and crack bridging.

Considering possible influences of strain gradients, there exists an inhomogeneous strain field with a strong gradient in plastic deformation ahead of the crack tip [56,57]. For the Ag/Cu−Zr micro-cantilevers, R_P is several times larger than individual layers, so the strain gradient within an individual layer will be small. Thus, we expect little influence on the failure behavior of the composite. However, for the Mo/Cu−Zr system, R_P is smaller than a single layer (<50 nm, see Fig. 6(b)). This could promote failure of individual layers, contributing to the low toughness. However, a detailed treatment of this aspect is beyond this work, as it would require a systematic variation of beam heights W.

4.2. Size and constituent dependent fracture toughness in C/ANL micro-cantilevers

Most investigations on fracture toughness of thin films are focused on hard but brittle coatings, such as TiN or TiN-based composited ceramic thin films [11,21,22], for improving their fracture performances. As the sample size is shrunk, a transition of stress state in front of the crack tip can occur (i.e., plane strain to plane stress) due to the change of boundary conditions, leading to a size-dependence of fracture toughness. This generally shows an initial increase from a constant value to a maximum followed by a pronounced drop with the sample thickness/width decreased to smaller scales [22,26,58]. For the tested size range of the presented C/ANLs micro-cantilevers, we just monitored a monotonous variation of fracture toughness K_Q with the cantilever width B, with completely inverse tendencies within the same size range. Classically, there are two critical sample sizes, B_1^* and B_2^*, differentiating the transition of stress state with changing sample width. B_1^* can be regarded as the plastic zone size R_P situated in plane strain (equation (3)), below which the plane stress condition fully develops. As the sample width is larger than another critical size $B_2^* = 2.5(K_Q/\sigma_y)^2$, the crack tip will be dominantly in plane strain condition, and fracture toughness tends to be a constant. Between B_1^* and B_2^*, both plane strain and plane stress co-exist around the crack tip as a mixed mode. For reference, these different regions are indicated in Fig. 6(a) and (b).

For the Mo/Cu−Zr micro-cantilevers, the fracture toughness K_Q first exhibits a stable minimum, and then gradually increased to ~1.5 MPa m$^{1/2}$ with reducing the beam width B, at approximately the transition in stress condition from plane strain to mixed mode at B_2^* ~1000 nm. This can be interpreted from the view of the energy release rate G during crack propagation, which is also equal to the crack propagation resistance R, i.e., $G = R = 2(\gamma_s + \gamma_p)$, where γ_s is the surface energy and γ_p the plastic dissipation energy. For all fractured samples, the surface energy can be treated as identical, while the contribution of plastic deformation may vary depending on the stress condition. In the case of ideal brittle fracture where only the energy required to break atomic bonds is spent during the crack propagation, no size dependence in the fracture energy is expected. Since the failure of Mo/Cu−Zr micro-beams is essentially brittle, we assume a defect controlled scenario. In the wider Mo/Cu−Zr cantilevers, we can observe some flaws induced by FIB-fabrication along the crack length (see Fig. 9(b)) that would initiate a Griffith crack, thus γ_p can be assumed to be zero. For a more slender beam, chances are reduced to have such a defect at or near the front of crack to cause the immediate crack propagation, i.e., $\gamma_p > 0$. Therefore, some plastic deformation in the slender Mo/Cu−Zr beam will take place, which contributes to the crack propagation resistance R and make the fracture toughness K_Q increase. This interpretation is supported by the calculated results of plastic zone size R_P in Mo/Cu−Zr cantilevers, which is on the order of the Mo grain size and much smaller than the beam width. The larger the plastic zone size R_P, the more plastic deformation energy the crack front dissipates, the more difficult the crack nucleation and propagation. With decreasing B, R_P gradually increased, implying that the crack propagation requires overcoming more resistance and inducing higher K_Q values.

The situation is completely different in the Ag/Cu−Zr case. Here, one would expect that the fracture toughness increases for smaller sample thicknesses, as in the case of macroscopic samples when the thickness is smaller than 10 times the plastic zone size. The reason for this behavior is that due to the reduction of the stress triaxiality in the plastic zone near the sample surface the initiation of pores is shifted to significantly larger strains, and the growth rate of pores is reduced compared to the plane strain case. The fracture process in the investigated nanolamellar Ag/Cu−Zr system is different. The Cu−Zr layers fracture at a certain strain, where breaking may start in the center of the sample, after which the cracks propagate through the whole layer to the surface. The propagation of the crack is then governed by the necking of the Ag layer, which as the ductile phase carries out plastic deformation by the emission of dislocations near the crack tip, while the amorphous Cu−Zr as hard and brittle metallic glass shows no blocking effect on crack propagation. Thus, the ductile Ag nanolayers primarily endow the C/ANLs beams considerable plasticity during bending, enhancing their fracture toughness. The necking to failure of the Ag layers under the constraint of adjacent Cu−Zr layers can be observed from the fractography (see Fig. 9(a)), and is at the root of the unexpected size-dependence of fracture toughness. In the wider Ag/Cu−Zr micro-beam, the Ag nanolayers deform like a sheet strongly constrained by the adjacent amorphous Cu−Zr layers. Once the crack starts to propagate from the notch, the Ag layer will require much more energy to get rid of the strong constraining effect for necking and be cut through by the crack. While in a more slender wire-like beam, the plastic deformation of Ag nanolayers is weakly constrained or even unconstrained by the neighboring Cu−Zr layers due to the reduced C/A interface contact. Thus, the input energy will be dominantly spent on forming new surface and growing the crack, instead of the plastic deformation of constituent layers, causing a lower fracture toughness. A similar fracture behavior was experimentally observed concerning the tensile ductility of aluminum alloys sheets, which decreased with reducing the specimen width [59]. In addition, a supporting argument arises from the change of the stress state during the blunting and necking process. As stated above, the conditional CTOD$_Q$ showed a drop from ~60 nm for the thicker beam to ~30 nm for the thinner one (see Fig. 7). Correspondingly, one would expect a reduction in fracture toughness, as observed in the present experiments in the Ag/Cu−Zr nanolaminates (see $K_{Q,CTOD}$ in Table 1), which further verifies the unusual size-dependent fracture toughness.

5. Conclusions

In this paper, fracture experiments on two kinds of pre-notched C/ANL micro-cantilevers, i.e., Ag/Cu−Zr and Mo/Cu−Zr with sample sizes ranging from several microns to the submicron scale, were conducted by *in-situ* bending tests in the SEM. The size-dependent fracture toughness and deformation mechanism were systematically investigated under different constituent constraints. The experimental results demonstrated higher fracture toughness in Ag/Cu−Zr C/ANLs which exhibited crack bridging in the Ag layers, while the Mo/Cu−Zr showed brittle fracture behavior and lower toughness values.

With reducing the cantilever width, the evaluated toughness value of Ag/Cu−Zr C/ANLs gradually decreased due to the size-dependent constraint effect on the deformation of the ductile Ag layers, whereas it increased in the Mo/Cu−Zr C/ANLs, which is attributed to a reduction in defect nucleation sites with reduced size.

The corresponding fracture behavior was closely related to the typical building blocks for enhancing the fracture resistance. For the Ag/Cu−Zr micro-cantilevers this was revealed to be the inter-connection of microcracks initiated in the amorphous Cu−Zr layers, while catastrophic crack extension was the underlying mechanism in Mo/Cu−Zr. The toughening mechanism of C/ANLs was attributed to plastic energy dissipation of ductile phases, crack tip blunting, crack bridging and the effect of a strain gradient in the plastic zone on crack propagation. These findings underline that care has to be taken when assessing fracture properties of layered low toughness structures, as the behavior might not be governed by simple linear elastic fracture mechanics and sample dimensions can significantly affect results. However, when conducted properly, these experiments provide a helpful guideline for progressive synthesis of nanoscaled crystalline/amorphous nanocomposite materials with high mechanical performance.

Acknowledgements

References

[1] R.O. Ritchie, The conflicts between strength and toughness, Nat. Mater. 10 (2011) 817−822.

[2] G. Liu, G.J. Zhang, F. Jiang, X.D. Ding, Y.J. Sun, J. Sun, E. Ma, Nanostructured high-strength molybdenum alloys with unprecedented tensile ductility, Nat. Mater. 12 (2013) 344−350.

[3] E. Ma, T. Zhu, Towards strength−ductility synergy through the design of heterogeneous nanostructures in metals, Mater. Today 20 (2017) 323−331.

[4] J. Wang, Q. Zhou, S. Shao, A. Misra, Strength and plasticity of nanolaminated materials, Mater. Res. Lett. 5 (2017) 1−19.

[5] A. Hohenwarter, B. Volker, M.W. Kapp, Y. Li, S. Goto, D. Raabe, R. Pippan, Ultra-strong and damage tolerant metallic bulk materials: a lesson from nano-structured pearlitic steel wires, Sci. Rep. 6 (2016) 33228.

[6] T.G. Nieh, J. Wadsworth, Hall-Petch relation in nanocrystalline solids, Scr. Metall. 25 (1991) 955−958.

[7] P.M. Anderson, C. Li, Hall-Petch relations for multilayered materials, Nano-structured Mater. 5 (1995) 349−362.

[8] A. Misra, J.P. Hirth, H. Kung, Single-dislocation-based strengthening mecha-nisms in nanoscale metallic multilayers, Philos. Mag. A 82 (2002) 2935−2951.

[9] A. Misra, J.P. Hirth, R.G. Hoagland, Length-scale-dependent deformation mechanisms in incoherent metallic multilayered composites, Acta Mater. 53 (2005) 4817−4824.

[10] J. Ast, M. Ghidelli, K. Durst, M. Göken, M. Sebastiani, A.M. Korsunsky, A review of experimental approaches to fracture toughness evaluation at the micro-scale, Mater. Des. 173 (2019) 107762.

[11] S.J. Suresha, S. Math, V. Jayaram, S.K. Biswas, Toughening through multi-layering in TiN−AlTiN films, Philos. Mag. 87 (2007) 2521−2539.

[12] Z.H. Xie, M. Hoffman, R.J. Moon, P.R. Munroe, Deformation of a hard coating on ductile substrate system during nanoindentation: role of the coating micro-structure, J. Mater. Res. 21 (2005) 437−447.

[13] L.W. Ma, J.M. Cairney, M. Hoffman, P.R. Munroe, Deformation mechanisms operating during nanoindentation of TiN coatings on steel substrates, Surf. Coat. Technol. 192 (2005) 11−18.

[14] Q. Zhou, S. Zhang, X. Wei, F. Wang, P. Huang, K. Xu, Improving the crack resistance and fracture toughness of Cu/Ru multilayer thin films via tailoring the individual layer thickness, J. Alloy. Comp. 742 (2018) 45−53.

[15] C.M. Lauener, L. Petho, M. Chen, Y. Xiao, J. Michler, J.M. Wheeler, Fracture of Silicon: influence of rate, positioning accuracy, FIB machining, and elevated temperatures on toughness measured by pillar indentation splitting, Mater. Des. 142 (2018) 340−349.

[16] J.P. Best, J. Wehrs, M. Polyakov, M. Morstein, J. Michler, High temperature fracture toughness of ceramic coatings evaluated using micro-pillar splitting, Scr. Mater. 162 (2019) 190−194.

[17] M. Sebastiani, K.E. Johanns, E.G. Herbert, G.M. Pharr, Measurement of fracture toughness by nanoindentation methods: recent advances and future chal-lenges, Curr. Opin. Solid State Mater. Sci. 19 (2015) 324−333.

[18] Z.H. Xie, M. Hoffman, P. Munroe, R. Singh, A. Bendavid, P.J. Martin, Micro-structural response of TiN monolithic and multilayer coatings during micro-scratch testing, J. Mater. Res. 22 (2007) 2312−2318.

[19] S.K. Venkataraman, D.L. Kohlstedt, W.W. Gerberich, Metal-ceramic interfacial fracture resistance using the continuous microscratch technique, Thin Solid Films 223 (1993) 269−275.

[20] K. Jonnalagadda, S. Cho, I. Chasiotis, T. Friedmann, J. Sullivan, Effect of intrinsic stress gradient on the effective mode-I fracture toughness of amorphous diamond-like carbon films for MEMS, J. Mech. Phys. Solids 56 (2008) 388−401.

[21] S. Massl, W. Thomma, J. Keckes, R. Pippan, Investigation of fracture properties of magnetron-sputtered TiN films by means of a FIB-based cantilever bending technique, Acta Mater. 57 (2009) 1768−1776.

[22] R. Hahn, M. Bartosik, R. Soler, C. Kirchlechner, G. Dehm, P.H. Mayrhofer, Superlattice effect for enhanced fracture toughness of hard coatings, Scr. Mater. 124 (2016) 67−70.

[23] P. Kontis, M. Köhler, S. Evertz, Y.T. Chen, V. Schnabel, R. Soler, J. Bednarick, C. Kirchlechner, G. Dehm, D. Raabe, J.M. Schneider, B. Gault, Nano-laminated thin film metallic glass design for outstanding mechanical properties, Scr. Mater. 155 (2018) 73−77.

[24] C. Motz, T. Schöberl, R. Pippan, Mechanical properties of micro-sized copper bending beams machined by the focused ion beam technique, Acta Mater. 53 (2005) 4269−4279.

[25] Y.-L. Kang, Z.-F. Zhang, H.-W. Wang, Q.-H. Qin, Experimental investigations of the effect of thickness on fracture toughness of metallic foils, Mater. Sci. Eng. A 394 (2005) 312−319.

[26] H.F. Li, P. Zhang, R.T. Qu, Z.F. Zhang, The minimum energy density criterion for the competition between shear and flat fracture, Adv. Eng. Mater. 20 (2018) 1800150.

[27] J. Ast, M. Göken, K. Durst, Size-dependent fracture toughness of tungsten, Acta Mater. 138 (2017) 198−211.

[28] S. Luo, Z. You, L. Lu, Thickness effect on fracture behavior of columnar-grained Cu with preferentially oriented nanoscale twins, J. Mater. Res. 32 (2017) 4554−4562.

[29] K. Matoy, H. Schönherr, T. Detzel, T. Schöberl, R. Pippan, C. Motz, G. Dehm, A comparative micro-cantilever study of the mechanical behavior of silicon based passivation films, Thin Solid Films 518 (2009) 247−256.

[30] K. Matoy, H. Schönherr, T. Detzel, G. Dehm, Micron-sized fracture experiments on amorphous SiOx films and SiOx/SiNx multi-layers, Thin Solid Films 518 (2010) 5796−5801.

[31] I. Radchenko, H.P. Anwarali, S.K. Tippabhotla, A.S. Budiman, Effects of interface shear strength during failure of semicoherent Metal−Metal nanolaminates: an example of accumulative roll-bonded Cu/Nb, Acta Mater. 156 (2018) 125−135.

[32] M. Huang, C. Xu, G. Fan, E. Maawad, W. Gan, L. Geng, F. Lin, G. Tang, H. Wu, Y. Du, D. Li, K. Miao, T. Zhang, X. Yang, Y. Xia, G. Cao, H. Kang, T. Wang, T. Xiao, H. Xie, Role of layered structure in ductility improvement of layered Ti-Al metal composite, Acta Mater. 153 (2018) 235−249.

[33] R. Raghavan, T.P. Harzer, V. Chawla, S. Djaziri, B. Phillipi, J. Wehrs, J.M. Wheeler, J. Michler, G. Dehm, Comparing small scale plasticity of copper-chromium nanolayered and alloyed thin films at elevated temperatures, Acta Mater. 93 (2015) 175−186.

[34] J. Buchinger, N. Koutná, Z. Chen, Z. Zhang, P.H. Mayrhofer, D. Holec, M. Bartosik, Toughness enhancement in TiN/WN superlattice thin films, Acta

Mater. 172 (2019) 18—29.

[35] I.J. Beyerlein, J. Wang, Interface-driven mechanisms in cubic/noncubic nano-laminates at different scales, MRS Bull. 44 (2019) 31—39.

[36] L.W. Yang, C. Mayer, N. Li, J.K. Baldwin, N.A. Mara, N. Chawla, J.M. Molina-Aldareguia, J. Llorca, Mechanical properties of metal-ceramic nanolaminates: effect of constraint and temperature, Acta Mater. 142 (2018) 37—48.

[37] B. Cheng, J.R. Trelewicz, Design of crystalline-amorphous nanolaminates using deformation mechanism maps, Acta Mater. 153 (2018) 314—326.

[38] Z. Fan, J. Li, Y. Yang, J. Wang, Q. Li, S. Xue, H. Wang, J. Lou, X. Zhang, "Ductile" fracture of metallic glass nanolaminates, Adv. Mater. Interfaces 4 (2017) 1700510.

[39] W. Guo, E.A. Jägle, P.-P. Choi, J. Yao, A. Kostka, J.M. Schneider, D. Raabe, Shear-induced mixing governs codeformation of crystalline-amorphous nano-laminates, Phys. Rev. Lett. 113 (2014) 035501.

[40] Y. Wang, J. Li, A.V. Hamza, T.W. Barbee Jr., Ductile crystalline-amorphous nanolaminates, Proc. Natl. Acad. Sci. 104 (2007) 11155—11160.

[41] M.P. Manoharan, A.V. Desai, M.A. Haque, Fracture toughness characterization of advanced coatings, J. Micromech. Microeng. 19 (2009) 115004.

[42] S. Wurster, R. Treml, R. Fritz, M.W. Kapp, E. Langs, M. Alfreider, C. Ruhs, P.J. Imrich, G. Felber, D. Kiener, Novel methods for the site specific preparation of micromechanical structures, Pract. Metallogr. 52 (2015) 131—146.

[43] R. Treml, D. Kozic, J. Zechner, X. Maeder, B. Sartory, H.P. Gänser, R. Schöngrundner, J. Michler, R. Brunner, D. Kiener, High resolution deter-mination of local residual stress gradients in single- and multilayer thin film systems, Acta Mater. 103 (2016) 616—623.

[44] F. Sadeghi-Tohidi, O.N. Pierron, Extreme stress gradient effects on micro-structural fatigue crack propagation rates in Ni microbeams, Appl. Phys. Lett. 106 (2015) 201904.

[45] D. Kiener, C. Motz, M. Rester, M. Jenko, G. Dehm, FIB damage of Cu and possible consequences for miniaturized mechanical tests, Mater. Sci. Eng. A 459 (2007) 262—272.

[46] S. Wurster, C. Motz, R. Pippan, Characterization of the fracture toughness of micro-sized tungsten single crystal notched specimens, Philos. Mag. 92 (2012) 1803—1825.

[47] Y.Q. Wang, K. Wu, J.Y. Zhang, G. Liu, J. Sun, Probing the size- and constituent-mediated mechanical properties and deformation behavior in crystalline/amorphous nanolaminates, Nanoscale 10 (2018) 21827—21841.

[48] M. Sistaninia, O. Kolednik, Improving strength and toughness of materials by utilizing spatial variations of the yield stress, Acta Mater. 122 (2017) 207—219.

[49] O. Kolednik, J. Predan, F.D. Fischer, P. Fratzl, Improvements of strength and fracture resistance by spatial material property variations, Acta Mater. 68 (2014) 279—294.

[50] ASTM Standard E 813-89, ASTM International, West Conshohochen, PA, 2003.

[51] J.J. Lewandowski, A.L. Greer, Temperature rise at shear bands in metallic glasses, Nat. Mater. 5 (2005) 15—18.

[52] Y.P. Li, G.P. Zhang, On plasticity and fracture of nanostructured Cu/X (X=Au, Cr) multilayers: the effects of length scale and interface/boundary, Acta Mater. 58 (2010) 3877—3887.

[53] J.W. Yan, X.F. Zhu, B. Yang, G.P. Zhang, Shear stress-driven refreshing capa-bility of plastic deformation in nanolayered metals, Phys. Rev. Lett. 110 (2013) 155502.

[54] C. Chen, J. Pascual, F. Fischer, O. Kolednik, R. Danzer, Prediction of the fracture toughness of a ceramic multilayer composite — modeling and experiments, Acta Mater. 55 (2007) 409—421.

[55] D. Kozic, H.P. Gänser, R. Brunner, D. Kiener, T. Antretter, O. Kolednik, Crack arrest in thin metallic film stacks due to material- and residual stress in-homogeneities, Thin Solid Films 668 (2018) 14—22.

[56] Y. Wang, J. Zhang, K. Wu, G. Liu, D. Kiener, J. Sun, Nanoindentation creep behavior of Cu—Zr metallic glass films, Mater. Res. Lett. 6 (2018) 22—28.

[57] W.D. Nix, H. Gao, Indentation size effects in crystalline materials: a law for strain gradient plasticity, J. Mech. Phys. Solids 46 (1998) 411—425.

[58] G. Dehm, B.N. Jaya, R. Raghavan, C. Kirchlechner, Overview on micro- and nanomechanical testing: new insights in interface plasticity and fracture at small length scales, Acta Mater. 142 (2018) 248—282.

[59] A.R. Shahani, M. Rastegar, M. Botshekanan Dehkordi, H. Moayeri Kashani, Experimental and numerical investigation of thickness effect on ductile fracture toughness of steel alloy sheets, Eng. Fract. Mech. 77 (2010) 646—659.